Ren, X, Huixin, Z and Qingxiang, Y

Insights into heterogeneous nucleation interface of Y2O3//NbN via first principles calculation

Insights into heterogeneous nucleation interface of Y_2O_3//NbN via first principles calculation

Huixin Zheng[a], Jibo Wang[b]*, Qizhen He[a], Yuenian He[a], Xuejun Ren[c], Qingxiang Yang[a]*

[a] *State Key Laboratory of Metastable Materials Science & Technology, Hebei key lab for optimizing metal product technology and performance, College of Materials Science & Engineering, Yanshan University, Qinhuangdao 066004, PR China* [b] *Fujian Provincial Key Laboratory of Welding Quality Intelligent Evaluation, Longyan University, Longyan 364012, People's Republic of China* [c] *School of Engineering, Liverpool John Moores University, Liverpool L3 3AF, UK*

*Corresponding author: Tel. +86-335-838-7471 Fax. +86-335-807-4545

E-mail address: wjb@lyun.edu.cn (J.B. Wang), qxyang@ysu.edu.cn (Q.X. Yang).

Abstract: The heterogeneous nucleation interface between Y_2O_3 and NbN was investigated by first principles method in this paper. The different low index interfaces mismatch degrees of Y_2O_3//NbN were calculated. Then, the interface models of Y_2O_3//NbN were constructed, and their interface properties were analyzed. The results show that the mismatch degree of Y_2O_3(111)//NbN(110) interface is the smallest, which is 7.61%. It reveals the effectiveness of Y_2O_3 as the heterogeneous nucleation nucleus of NbN is medium. Four interface models of Y_2O_3(111)//NbN(110) interface are constructed, namely Y-NbNⅠ, Y-NbNII, O-NbNⅠ and O-NbNII interfaces. Among them, the adhesive work of O-NbNII interface is the largest, which is 6.26J/m^2, and its interface energy is the smallest, which is -3.08J/m^2. The O-NbNII interface mainly involves the binding of N-Y, Nb-O ionic bonds, and N-O covalent bonds. Therefore, Y_2O_3 can serve as the heterogeneous nucleation nucleus of NbN, and the O-NbNII interface is the most stable one.

Keywords: Y_2O_3; NbN; First principles; Interface; Heterogeneous nucleation

1. Introduction

With specific features such as the active chemical properties, low potential, and special electronic layer arrangement, the rare earth (RE) elements can almost interact

with any element [1-3]. At present, RE elements have been widely applied in various alloys, to refine their structure and improve the physical and mechanical properties [46]. Yang et al. [7] added element Gd to AM50 magnesium alloy. The results showed that after adding element Gd, its grain size is significantly refined, and the tensile strength and corrosion resistance can be improved. Wang et al. [8] studied the effect of element Ce on the mechanical property of NiAl alloys, and found that the hardness and ductility of NiAl have been improved by element Ce.

As the first discovered RE element, element Y has been widely applied in materials science. Li et al. [9] studied the effect of the Y content on the migration of twin boundaries in Mg alloys. It was found that with the increase of Y content, the migration speed of the twin boundaries is increased. Qin et al. [10] alloyed $ZrFe_2$ with Y to obtain $Zr_{1-x}Y_xFe_2$ (x¼0.1e0.4) compounds and studied its microstructure and hydrogen storage performance. It was found that doping with Y element could improve the hydrogen storage capacity.

Currently, because of its stable structure, obtained in nature easily, Y_2O_3 has been widely used in alloys to replace element Y to improve the comprehensive properties of alloys. Shu et al. [11] found that the W_f/W composites with Y_2O_3 coating could effectively prevent the recrystallization and abnormal grain growth of the fiber in the sintering process, and improve its strength. Xing et al. [12] found that the microstructure of Ni-W nanocrystalline alloy coating can be refined and its corrosion resistance improved due to the addition of Y_2O_3 nanoparticles.

Due to their high hardness, high melting point, stable chemical properties, and good conductivity, nitrides have attracted widespread attention [13]. N atoms can combine with micro-alloyed elements Ti and Nb to form specific nitrides TiN and NbN [14]. TiN and NbN are often used as strengthening phases in various alloys or surface coatings because of their excellent physical and chemical properties [15-17]. Vinolia et al. [18] studied the effect of NbN addition on the mechanical properties of TiAl, and found that it can improve the microhardness of TiAl-NbN composite materials. Papken [19] verified the strengthening effect of TiN/NbN superlattice coatings on CoCrMo alloy matrix by analyzing the local load bearing capacity of TiN/NbN superlattice coatings and the subsequent crack formation mechanism.

With excellent wear resistance, the hypereutectic Fe-Cr-C alloy has been widely applied in additive manufacturing industry [20]. In hypereutectic Fe-Cr-C alloy, it has been found that its microstructure can be further refined and the wear resistance further improved when Y_2O_3 and NbN were added in this alloy simultaneously, compared with that when Y_2O_3 and NbN were added in this alloy respectively [21,22]. The reason may be that Y_2O_3 can serve as the heterogeneous nucleation nucleus of NbN, to refine NbN and further refine the microstructure of the hypereutectic Fe-Cr-C alloy. However, because of the small size of Y_2O_3 and NbN, the refining mechanism of NbN by Y_2O_3 is difficult to explain clearly by experiment.

The first principles method based on density functional theory has become a research hotspot and has been widely applied in materials interface. Cheng et al. [23] calculated the interface energy and adhesion work of different stacking models of Ni_3Al-Ni_3Ta by using first principles method. It found that the polar interface terminated by Ni atom was the most stable, with the largest adhesion work and the smallest interface energy. Li et al. [24] studied the low-exponential interface configuration, interface energy and electronic properties of the NbN/α-Fe interface in ship-building steel by using first principles method, and revealed the stable binding mode and position orientation relationship of the NbN/α-Fe interface in steel, which can provide theoretical guidance for refining the NbN grains in ship-building steel. Therefore, it is feasible to establish Y_2O_3//NbN interface model and elucidate its heterogeneous nucleation mechanism by first principles calculation.

The different low index interfaces mismatch degrees between Y_2O_3 and NbN were calculated in this paper. The interface with the minimum mismatch of Y_2O_3//NbN was selected to construct interface model by first principles method. And their interface properties were analyzed. The effectiveness of Y_2O_3 as the heterogeneous nucleation nucleus of NbN was analyzed.

2. Calculation details

The first principles calculation method based on density functional theory for simulation calculations was adopted in this paper, and all calculations were carried out using the Vienna Ab initio Simulation Package (VASP) software [25]. The exchange correlation functional between particles was described using the perdew burke

ernzerhof (PBE) functional under the generalized gradient approximation (GGA) [26], and the interaction between electrons was handled by the projection augmented plane wave (PAW) method [27].

The selected crystal structure model for calculation is shown in Fig. 1. Fig. 1 (a) is the crystal structure of NbN, in which, the green balls represent N atoms and blue ones represent Nb atoms. It's a sodium chloride type structure. Before optimization, the lattice constant is a=b=c=4.416Å, α=β=γ=90°. After optimization, the lattice constant is a=b=c=4.448Å, α=β=γ=90°. Fig. 1(b) is the crystal structure of Y_2O_3, in which, the blue balls represent Y atoms and red ones represent O atoms. It is a fluorite type structure with disordered oxygen vacancies. Before optimization, the lattice constant is a=b=c=5.264Å, α=β=γ=90°. After optimization, the lattice constant is a=b=c=5.431Å, α=β=γ=90°. Energy and force converge to 1×10^{-5}eV/atom and 0.01eV/Å during the process of the structure optimization.

The K point and truncation energy (Encut) of NbN with different energy are shown in Fig. 2. Fig. 2(a) is the K point of NbN with different energy. The energy converges when the K point is set to 9*9*9. Fig. 2(b) is the Encut of NbN with different energy. The energy converges when the Encut reaches 420eV. Therefore, K point and Encut of NbN are set to 9*9*9 and 420eV, respectively.

The K point and Encut of Y_2O_3 with different energy are shown in Fig. 3. Fig. 3(a) is the K point of Y_2O_3 with different energy. The energy converges when the K point is set to 8*8*8. Fig. 3(b) is the Encut of Y_2O_3 with different energy. The energy converges when the Encut reaches 500eV. Therefore, K point and the Encut of Y_2O_3 are set to 8*8*8 and 500eV, respectively.

3. Bulk phase and mechanical properties

3.1. Bulk phase properties

The bulk phase properties of NbN are shown in Fig. 4. Fig. 4 (a) is the band structure diagram of NbN, and the dashed line position is the Fermi level. The energy band of NbN passes through the Fermi level, and there is no energy gap between the conduction band and the valence band, which indicates that NbN has certain metallic

characteristics. Fig. 4 (b) is the density of state (DOS) diagram of NbN, and the dashed line position is the Fermi level. The valence band is mainly the N-p orbital contribution, and the conduction band is the Nb-d orbital contribution, which indicates the existence of metallic bond in NbN. In the range of -8~-3eV, N-p orbital and Nb-d orbital peak patterns are basically the same, and there is a certain degree of resonance between them, which indicates that N-Nb covalent bond is formed. Therefore, the chemical bond of NbN is a combination of metallic bond and covalent bond.

The bulk phase properties of Y_2O_3 are shown in Fig. 5. Fig. 5(a) is the band structure of Y_2O_3, and the dashed line is the Fermi level. It can be seen that there is a band passing through the Fermi level, while there is a band gap of about 5eV between the conduction band and the valence band, which indicates that Y_2O_3 has the property of a wide-band gap semiconductor. Fig. 5(b) is DOS diagram of Y_2O_3, and the dashed line position is the Fermi level. The conduction band is mainly the Y-d orbital contribution, and the valence band is mainly the O-p orbital contribution. Y-d orbitals interact with O-p orbitals in the range from -3.7eV to Fermi level. The peaks at the Fermi level are mainly O-P orbitals, and the peak density of Y-D orbitals is very low, which indicates that the electrons of Y atoms are transferred to O atoms in Y_2O_3, forming Y-O ionic bonds. In the range -21eV to -13.5eV, Y-d orbitals interact with O-s orbitals, so the main form of bonding in Y_2O_3 is ionic bond.

3.2. Elastic property

The volume modulus, shear modulus, Young's modulus and Poisson's ratio of NbN and Y_2O_3 were calculated using the stiffness matrix C_{ij}. The calculation results are as follow.

The elastic matrix of NbN is calculated as follow:

$$C_{ij}(GPa) = \begin{vmatrix} 629.03 & 158.17 & 158.17 & & & \\ 158.17 & 629.03 & 158.17 & & & \\ 158.17 & 158.17 & 629.03 & & & \\ & & & 80.435 & & \\ & & & & 80.435 & \\ & & & & & 80.435 \end{vmatrix}$$

The elastic matrix of Y_2O_3 is calculated as follow:

$$C_{ij}(GPa) = \begin{vmatrix} 88.381 & 171.31 & 171.31 & & & \\ 171.31 & 88.381 & 171.31 & & & \\ 171.31 & 171.31 & 88.381 & & & \\ & & & 48.086 & & \\ & & & & 48.086 & \\ & & & & & 48.086 \end{vmatrix}$$

The elastic constants of NbN and Y_2O_3 using the stiffness matrix are listed in Table 1. The anisotropy of the NbN elastic constant is listed in Table 2. The 3D and 2D maps of elastic anisotropy drawn according to the NbN stiffness matrix are shown in Fig. 6.

Table 1 Elastic constants of NbN and Y_2O_3

	Bulk modulus	Shear modulus	Young's modulus	Poisson's ratio
	K	G	E	μ
NbN	311.88	109.67	294.49	0.34
Y_2O_3	144.3	167.88	362.9	0.081

Table 2 Anisotropy of the NbN elastic constant

	Young's modulus (GPa)		Linear coefficient (TPa^{-1})		Shear modulus (GPa)		Poisson's ratio	
	E_{min}	E_{max}	β_{min}	β_{max}	G_{min}	G_{max}	μ_{min}	μ_{max}
NbN	222.38	565.47	1.0129	1.0129	90.435	235.43	0.09315	0.62956
Anisotropy	2.543		1.0000		2.927		6.7585	

It can be seen that the three-dimensional image of the linear compression coefficient of NbN is a very regular spherical shape, while the two-dimensional image in all directions is also a regular circular shape. The maximum and minimum values of

the linear compression coefficient are equal, both are 1.0578, and the anisotropy is 1.0, which indicates that the linear compression coefficient of NbN is isotropic. The threedimensional graphs of shear modulus, Young's modulus and Poisson's ratio are irregular stereograms. The minimum shear modulus is 222.38GPa, the maximum shear modulus is 565.47GPa, and the anisotropy is 2.543; The minimum shear modulus is 90.435GPa, the maximum shear modulus is 235.43GPa, and the anisotropy is 2.927. The minimum value of Poisson's ratio is 0.09315, the maximum value is 0.62956, and the anisotropy is 6.7585.

The calculations of elastic anisotropy, 3D and 2D maps of Y_2O_3 were no longer made as its mechanical instability.

4. Lattice mismatch degree

According to Bramfitt two-dimensional lattice mismatch theory [28], when the lattice mismatch degree between Y_2O_3 and NbN is more than 12%, Y_2O_3 can't be used as heterogeneous nucleation, while between 6% and 12%, it belongs to the range of medium effective nucleation, and within 6%, it belongs to the range of effective nucleation. The formula for two-dimensional lattice mismatch is as follow [28]:

$$\delta_{(hkl)_n}^{(hkl)_s} = \sum_{i=1}^{3}\left[\left(d_{[uvw]_s}^{i}\cos\theta - d_{[uvw]_n}^{i}\right)/d_{[uvw]_n}^{i}\right)/3]\times 100\%)] \quad (1)$$

where, $(hkl)_s$is the low exponential plane in the nucleating basement; $[uvw]_s$ is a low exponential direction on$(hkl)_s$; $d_{[uvw]s}$is the atomic spacing along the direction of$[uvw]_s$; $(hkl)_n$is the low exponential plane of the nucleation phase; $[uvw]_n$ is a low exponential direction on $(hkl)_n$; $d_{[uvw]n}$ is the atomic spacing along the direction of$[uvw]_n$; θ is the angle between $[uvw]_s$and $[uvw]_n$.

Two groups of low exponential planes, Y_2O_3(111)//NbN(110) and Y_2O_3(110)//NbN(111), were selected to calculate their interface mismatch degree, and the results are listed in Table 3.

Table 3 Lattice mismatch degree between Y_2O_3 and NbN

Matching face	Y_2O_3(111)//NbN(110)	Y_2O_3(110)//NbN(111)

Y_2O_3[uvw]	[1$\bar{1}$0]	[1$\bar{1}$2]	[1$\bar{1}$1]	[1$\bar{1}$2]	[$\bar{1}$11]	[$\bar{1}$14]
NbN[uvw]	[001]	[1$\bar{1}$0]	[1$\bar{1}$1]	[1$\bar{1}$0]	[1$\bar{1}$2]	[10$\bar{1}$]
θ(°)	0	0	5.264	0	0	5.264
d_{Y2O3}(Å)	3.84	6.652	7.681	6.652	9.407	11.522
d_{NbN}(Å)	4.48	6.29	7.704	6.254	10.816	12.489
δ(%)		7.61			8.65	

It can be seen that the mismatch degree of Y_2O_3(111)//NbN(110) interface is 7.61%, and that of Y_2O_3(110)//NbN(111) interface is 8.65%, both of them are less than 12%, which indicates that Y_2O_3 is medium effective as the heterogeneous nucleation nucleus of NbN. Therefore, Y_2O_3(111) and NbN(110) planes with low mismatch (7.61%) was selected to construct the surface and interface models.

5. Interface properties

5.1. Surface convergence

According to the calculation results of two-dimensional lattice mismatch degree, Y_2O_3(111) and NbN(110) planes were selected to construct a surface model, and the convergence of surface energy was tested. There are three terminating surface models for Y_2O_3(111) plane, namely Y-terminated, O1-terminated and O2- terminated surface models. There is one surface model for the NbN(110) plane. The thickness of the selected vacuum layer is 15 Å. The four surface models constructed are shown in Fig. 7.

Y_2O_3(111) plane is a polar one, and the chemical potential of its surface model can be calculated as follow [29]:

$$\mu_{Y_2O_3}^{bulk} = 2\mu_Y + 3\mu_O \tag{2}$$

where, $\mu_{Y_2O_3}^{bulk}$ is the system energy of Y_2O_3(111) plane; μ_Y is the chemical potential of the Y atoms; μ_O is the chemical potential of the O atoms.

The surface energy of Y_2O_3 can be calculated as follow [29]:

$$\sigma_{Y_2O_3(111)} = \frac{1}{2A}(E_{slab} - N_Y\mu_Y - N_O\mu_O) \tag{3}$$

where, $\sigma_{Y_2O_3(111)}$is the surface energy of Y_2O_3(111) plane; $E_{slab}$is the energy value of the surface model with a certain number of atomic layers; A is the surface area of the surface model; N_Y and N_O are the number of Y and O atoms in the surface model.

For the surface model of Y-terminated, the formula is as follow:

$$N_O = 2N_Y - 4 \quad (4)$$

For the surface model of O1-terminated, the formula is as follow:

$$N_O = 2N_Y - 4 \quad (5)$$

For the surface model of O2-terminated, the formula is as follow:

$$N_O = 2N_Y + 4 \quad (6)$$

Equations (2), (3) and (4) are combined to obtain the final surface energy calculation formula of Y_2O_3(111) surface model of Y-terminated as follow:

$$\sigma_{Y_2O_3(111)} = \frac{1}{2A}\left[E_{slab} - \frac{1}{2}N_Y\mu_{Y_2O_3}^{bulk} - \frac{1}{2}N_Y\mu_O\right] \quad (7)$$

Equations (2), (3) and (5) are combined to obtain the final surface energy calculation formula of Y_2O_3(111) surface model of O1-terminated as follow:

$$\sigma_{Y_2O_3(111)} = \frac{1}{2A}\left[E_{slab} - \frac{1}{2}N_Y\mu_{Y_2O_3}^{bulk} - \left(\frac{1}{2}N_Y - 4\right)\mu_O\right] \quad (8)$$

Equations (2), (3) and (6) are combined to obtain the final surface energy calculation formula of Y_2O_3(111) surface model of O2-terminated as follow:

$$\sigma_{Y_2O_3(111)} = \frac{1}{2A}\left[E_{slab} - \frac{1}{2}N_Y\mu_{Y_2O_3}^{bulk} - \left(\frac{1}{2}N_Y + 4\right)\mu_O\right] \quad (9)$$

The surface model of Y_2O_3(111) plane is polar one. The surface energy calculation results of Y_2O_3(111) surface model of Y-terminated are shown in Table 4. When the number of surface layers reaches 13, the surface energy of Y_2O_3(111) surface model of Y-terminated can converge to 0.59J/m^2. The surface energy calculation results of Y_2O_3(111) surface model of O1-terminated are shown in Table 5. When the number of surface model layers reaches 9, the surface energy of Y_2O_3(111) surface model of O1terminated can converge to 0.69J/m^2. The surface energy calculation results of Y_2O_3(111) surface model of O2-terminated are shown in Table 6. The model is unstable, because the surface energy of the Y_2O_3(111) surface model of O2-terminated is negative.

Table 4 Surface energy of Y_2O_3(111) surface model of Y-terminated

Layer	4	7	10	13	16

Y_2O_3(111)	3.76	1.27	0.54	0.59	0.58

Table 5 Surface energy of Y_2O_3(111) surface model of O1-terminated

Layer	3	6	9	12	15
Y_2O_3(110)	0.81	0.69	0.69	0.68	0.67

Table 6 Surface energy of Y_2O_3(111) surface model of O2-terminated

Layer	5	8	11	14	17
Y_2O_3(110)	-0.81	-1.18	-1.32	-1.19	-1.12

The NbN(110) plane is a non-polar one, and the surface energy calculation formula of the surface model using Botteger formula is as follows [30]:

$$\sigma_{NbN(110)} = \frac{1}{2A}(E_{slab}^{N} - N\Delta E) \quad (10)$$

$$\Delta E = (E_{slab}{}^{N} - E_{slab}{}^{N-2})/2 \quad (11)$$

where, $\sigma_{NbN(110)}$ is the surface energy of NbN(110) plane; $E_{slab}{}^{N}$ is the energy value of the NbN(110) surface model containing N layer atoms; E_{slab}^{N-2} is the energy value of the NbN(110) surface model containing N-2 layer atoms; N is the number of atomic layers of the surface model。

The surface energy calculation results of NbN(110) plane are listed in Table 7. It can be seen that the non-polar surface of NbN(110) plane can converge to 2.67J/m^2 when the number of model layers of the surface reaches 11.

Table 7 Surface energy of NbN(110) plane

Layer	5	7	9	11	13
NbN(110)	2.4	2.54	2.73	2.67	2.69

5.2. Interface model constructure

On the basis of the lattice mismatch degree and surface convergence tests, four interface models of Y_2O_3(111)//NbN(110) interface were constructed considering different stacking methods, as shown in Fig. 8. The OT interface containing a Y terminating surface in Y_2O_3(111)//NbN(110) interface is named Y-NBN Ⅰ model, where Nb and N atoms are directly opposite to Y atoms. The HCP interface containing a Y terminating surface in Y_2O_3(111)//NbN(110) interface is named Y-NBNII model, where Nb and N atoms on the bridge site of Y atoms. The OT interface with O1

terminating surface in Y_2O_3(111)//NbN(110) interface is named O-NBN Ⅰ model, where Nb and N atoms are directly opposite to O atoms. The HCP interface containing a O1 terminating surface in Y_2O_3(111)//NbN(110) interface is named O-NBNII model, where Nb and N atoms on the bridge site of O atoms. The four interface models are relaxed, and the energy variations of the four interface models with the interface spacing are shown in Fig. 9. It can be seen that the energy of Y-NbN Ⅰ interface model is the lowest when the interfacial distance is 2.8Å. That of Y-NbNII interface model is the lowest when the interfacial distance is 2.6 Å. That of O-NbN Ⅰ interface model is the lowest when the interfacial distance is 2.2Å. That of O-NbNII interface model is the lowest when the interfacial distance is 2.2Å.

5.3. Interface adhesive work and interface energy

Adhesive work (W_{ad}) and interface energy (γ) can be used to judge the bonding strength and stability of the interface, and they are also related to the electronic structure and bonding properties of the interface.

W_{ad} is an important parameter to characterize the bonding strength of interface. Among them, the formula W_{ad} for Y_2O_3(111)//NbN(110) is as follow [31]:

$$W_{ad} = \frac{1}{A}(E_{Y_2O_3} + E_{NbN} - E_{Y_2O_3/NbN}) \quad (12)$$

where, A is the interface area; E_{Y2O3} is the energy of Y_2O_3(111) surface model; E_{NbN} is the energy of the NbN(110) surface model; $E_{Y2O3/NbN}$ is the energy of the Y_2O_3(111)//NbN(110) interface model.

γ is the resistance of heterogeneous interfacial nucleation, and the number of interface energy corresponds to the difficulty of heterogeneous interfacial nucleation. The formula γ for Y_2O_3(111)//NbN(110) interface model is as follow [32]:

$\gamma = \sigma_{Y2O3} + \sigma_{NbN} - W_{ad}$ (13) where, $\sigma_{Y2O3}$is the surface energy of Y_2O_3(111) surface model; σ_{NbN} is the surface energy of the NbN(110) surface model.

The calculated W_{ad} and γ of four Y_2O_3(111)//NbN(110) interface models are listed in Table 8. The W_{ad} order of the four interface models is as follow: $W_{adO\text{-}NbNII} > W_{adO\text{-}NbN\,I} > W_{adY\text{-}NbNII} > W_{adY\text{-}NbN\,I}$. The γ of the four interface models is as follow: $\gamma_{O\text{-}NbNII} < \gamma_{O\text{-}NbN\,I} < \gamma_{Y\text{-}NbNII} < \gamma_{Y\text{-}NbN\,I}$. The W_{ad} of O-NbNII interface is the largest, which is 6.26J/m^2. Meanwhile, the γ of O-NBNII interface is the smallest, which is -3.08J/m^2. Therefore, the O-NBNII interface is the most stable.

Table 8 W_{ad} and γ of four Y_2O_3(111)//NbN(110) interface models

Interface model	Y-NbN Ⅰ	Y-NbNII	O-NbN Ⅰ	O-NbNII
W_{ad}(J/m^2)	-9.47	-9.22	-1.67	6.26
γ(J/m^2)	13.82	13.57	4.85	-3.08

6. Interface model bonding

The bonding of interface model can be analyzed by using charge density, differential charge density and electron local function (ELF). The calculation formula of differential charge density is as follow [33]:

$$\rho_d = \rho_{tot} - \rho_{Y_2O_3} - \rho_{NbN} \quad (14)$$

where, ρ_{tot} is the total charge density in the interface model; $\rho_{Y_2O_3}$ is the charge density of Y_2O_3(111); ρ_{NbN} is the charge density of NbN(110).

The charge densities of the four interface models along the (100) cutting plane are shown in Fig. 10. The region of the charge accumulation is represented by red color and that of the charge depletion is represented by blue color. The charge density is increasing from blue region to red region. Fig. 10 (a) is the charge density of the YNbN Ⅰ interface. The charge density around the O atoms is the highest, and the charge density around the Y atoms is the lowest, which indicates that the O atoms have a strong ability to gain electrons, and the Y atoms loses electrons. Meanwhile, Nb and O atoms diffuse towards the interface, and the charge density around O atoms is higher than that around Nb atoms, which indicates that the interaction between Nb and O atoms is stronger. Fig. 10 (b) is the charge density of the Y-NBNII interface. The charge density around the O atoms is the highest, and the charge density around the Y atoms is the lowest, which indicates that the O atoms have a strong ability to gain electrons, and the Y atoms lose electrons. Meanwhile, N and Y atoms diffuse towards the interface, and the charge

density of N atoms is higher than that of Y atoms, which indicates that N atoms have stronger electron generating ability than Y atoms. Fig. 10 (c) is the charge density of the O-NbNI interface. The charge density around the O atoms is the highest, and the charge density around the Y atoms is the lowest, which indicates that the O

atoms gain electrons and the Y atoms lose electrons. Meanwhile, O and Nb atoms diffuse towards the interface. The charge overlaps around the O and Nb atoms, which indicates that a strong chemical bond is formed between the O and Nb atoms. Fig. 10 (d) is the charge density of the O-NBNII interface. The charge density around the O atoms is still the highest, and the charge density around the Y atoms is the lowest, which indicates that the O atoms gain electrons and the Y atoms lose electrons. Meanwhile, the diffusion of O and Nb atoms is more obvious, and there is an overlapping region of charges around the two kinds of atoms, which indicates that the chemical bond formed between the two is stronger.

The ELF value is between 0 and 1. When ELF=1, it indicates that the electrons are completely localized; When ELF=1/2, it indicates a uniform electron gas state. And when ELF=0, it indicates that the electrons are completely delocalized or there are no electrons present at all.

The ELF distributions of the Y_2O_3(111)//NbN(110) interface model are shown in Fig. 11. Fig. 11(a) is the ELF distribution on the Y-NbNI interface. The ELF value around the O atoms is about 0.8, which indicates that the electrons around them are in a localized state. The ELF value around the Nb atoms is about 0.3, and the ELF value between the Nb and O atoms is about 0.2, which indicates the formation of ionic bonds. Fig. 11(b) is the ELE distribution at the Y-NBNII interface. The ELF value around the N atoms is about 0.8, which indicates that the N atoms are in in a localized state. The ELF value around the Y atoms is about 0.4, which corresponds to the charge density diagram. The ELF value between the N and Y atoms at the interface ranges from 0 to 0.2, which indicates the formation of ionic bonds. Fig. 11(c) is the ELF distribution at the O-NbNI interface. The ELF value around the O atoms is about 0.8, which indicates that the electrons around the O atoms are in a localized state, the ELF value around the Nb atoms is about 0.4, and the ELF value between the Nb and O atoms is about 0.3, which indicates that ionic bonds are formed between them. Fig. 11(d) is the ELF

distribution at the O-NBNII interface. The ELF value around the O atoms is about 0.8, which indicates that the electrons around the O atoms are in a localized state. The ELF value around the Nb atoms is about 0.4, and the ELF value between the Nb and O atoms is about 0.3, which indicates that ionic bonds are formed between them.

The differential charge densities of the Y_2O_3(111)//NbN(110) interface model along the (100) cutting plane are shown in Fig. 12. Fig. 12(a) is the differential charge density of the O-NbNI interface. The charge density around Nb atoms is decreased and the charge density around O atoms is increased at the interface, and an ionic bond is formed between them. Fig. 12(b) is the differential charge density of the O-NbNII interface model.The charge density around Nb atoms is decreased and the charge density around O atoms is increased at the interface, and an ionic bond is formed between them. It can be seen that there are more Nb atoms and O atoms relax to the interface compared with the O-NbNI interface model. Therefore, the ionic bond strength formed is higher and the interface bond is more stable than the O-NbNI interface model.

The partial densities of the states (PDOS) of the four interface models are shown in Fig. 13. All four kinds of interfaces have peaks near Fermi level, and the peaks near Fermi level are mainly Nb-d and O-p orbits, which indicates that these four interfaces have metallic characteristics. Fig. 13(a) is the PDOS of Y-NbNI interface model. In the range of -22~-19.8eV, both N-d and Y-p orbitals have strong peaks at the interface, which indicates that chemical bonds are formed between them. In the range of 16.8~14.8eV, both N-s and O-s orbitals have strong peaks, and the peak intensity of the two orbitals is similar, which indicates that covalent bonds are formed between them. In the range of -5~0eV, Nb-p, Nb-d and N-p orbitals mainly interact with O-p orbitals, and the peak intensity of O-p orbitals is higher, which indicates the formation of N-O and Nb-O bonds. Fig. 13(b) is the PDOS of Y-NbNII interface. In the range of -22.8~21.4eV, Y-p orbital and N-p orbital resonance phenomenon, and Y-p orbital peak intensity is higher, which indicates the formation of N-Y ionic bonds. In the range of 17~-14eV, both N-s and O-s orbitals have strong peaks, and the peak intensity of the two orbitals is similar, which indicates that covalent bonds are formed between N and O atoms. In the range of -16.8~14.8eV, both N-S and O-S orbitals have strong peaks, and the peak intensity of the two orbitals is similar, which indicates that covalent bonds

are formed between N and O atoms. In the range of -5~-3eV, Nb-d and N-p orbitals mainly interact with O-p orbitals, and the peak intensity of O-p orbitals is higher, which indicates the formation of N-O and Nb-O bonds. Fig. 13(c) is the PDOS of O-NbN Ⅰ interface. In the range of -22.8~-21.4eV, Y-p orbital and N-p orbital resonance phenomenon, and Y-p orbital peak intensity is higher, which indicates the formation of N-Y ionic bonds. In the range of -17~-14eV, both N-s and O-s orbitals have strong peaks, and the peak intensity of the two orbitals is similar, which indicates that covalent bonds are formed between N and O atoms. In the range of -5~-3eV, Nb-d and N-p orbitals and O-p orbitals mainly interact, and the peak strength of the O-p orbitals is higher than that of the Nb-d orbitals, which indicates that the ionic bonds are formed between Nb and O atoms, and the peak strength of the N-p orbitals and O-p orbitals is similar, which indicates that the covalent bonds are formed between them. In the range of -3~0eV, Nb-d orbit and O-p orbit mainly interact, and the peak intensity of the O-p orbit is higher than that of the Nb-d orbit, which indicates that the ionic bonds between Nb-O are formed. Fig. 13(d) is the PDOS of O-NbNII interface. In the range of -22.8~21.4eV, Y-p orbital and N-p orbital resonance phenomenon, and Y-p orbital peak intensity is higher, which indicates the formation of N-Y ionic bonds. In the range of 17~-14eV, both N-S and O-S orbitals have strong peaks, and the peak intensity of the two orbitals is similar, which indicates that covalent bonds are formed between N and O atoms. In the range of -7~-3eV, Nb-d, N-p and O-p orbits mainly interact, and the peak strength of the O-p orbit is higher than that of the Nb-d orbit, which indicates that the ionic bonds are formed between the Nb-O orbits, and the peak strength of the N-p and O-p orbits is similar, which indicates that the covalent bonds are formed between them. In the range of -3~0eV, Nb-d orbit and O-p orbit mainly interact, and the peak intensity of the O-p orbit is higher than that of the Nb-d orbit, which indicates that the ionic bonds between Nb-O is formed.

7. Discussion on heterogeneous nucleation mechanism

According to the results of Bramfitt two-dimensional lattice mismatch theory, the lattice mismatch degree of Y_2O_3(111) and NbN(110) is the smallest, which is 7.61%. It indicates that Y_2O_3 is medium effective as heterogeneous nucleation nucleus of NbN. According to the calculation results of adhensive work and interface energy of

Y_2O_3(111) and NbN(110), the adhesive work of O-NbNII interface model is the largest, which is 6.26J/m^2, and its interface energy is the smallest, which is -3.08J/m^2. It indicates that the nucleation resistance of O-NbNII interface model is relatively small, and the formed interface is stable. According to the analysis of charge density and state density, the O-NbNII interface model is mainly composed of N-Y, Nb-O ionic bonds and N-O covalent bonds. Therefore, among the heterogeneous nucleation interfaces of Y_2O_3(111) and NbN(110), the O-NbNII interface model is the most stable.

8. Conclusion

1. The crystal structure of Y_2O_3 and NbN is optimized. The Encut of Y_2O_3 is 500eV, and the K point is 8*8*8. The Encut of NbN is 420eV, and the K point is 9*9*9.

2. NbN has metal characteristics and its chemical bonds are mainly metallic bonds and Nb-N covalent bonds. Y_2O_3 has the properties of a wide-band gap semiconductor, and its chemical bond is Y-O ionic bond.

3. The bulk modulus K of NbN is 311.8GPa. The shear modulus G is 109.67GPa; Young's modulus E is 294.49GPa; Poisson's ratio is 0.34; The linear compression coefficient is isotropic, while the shear modulus, Young's modulus and Poisson's ratio are anisotropic. The bulk modulus K of Y_2O_3 is 144.3GPa. The shear modulus G is 167.88 GPa; Young's modulus E is 362.9GPa; Poisson's ratio was 0.081.

4. The crystal mismatch degree between Y_2O_3(111) plane and NbN(110) plane is the smallest (7.61%), which indicates that Y_2O_3 is medium effective as heterogeneous nucleation nucleus of NbN.

5. Y_2O_3(111) plane and NbN(110) plane are selected for surface model construction and surface convergence test. When the number of surface model layers of NbN(110) reaches 11 layers, the surface energy converges at 2.67J/m^2.When the number of surface layers reaches 13, the surface energy of Y_2O_3 (111) surface model of Y-terminated can converge to 0.59J/m^2. When the number of surface model layers reaches 9, the surface energy of Y_2O_3 (111) surface model of O1-terminated can converge to 0.69J/m^2.

6. The adhesive work of O-NBNII interface model is the largest, which is 6.26J/m^2, and its interface energy is the smallest, which is -3.08J/m^2. Therefore, the O-NbNII interface is the most stable.

7. The four interface structures are mainly N-Y, Nb-O ionic bonds and N-O covalent bonds.

Acknowledgements

The authors would like to express their gratitude for projects supported by the National Natural Science Foundation of China (No. 52371077).

Reference

[1] J. Bohlen, S. Yi, D. Letzig, K.U. Kainer, Effect of rare earth elements on the microstructure and texture development in magnesium–manganese alloys during extrusion[J], Mater. Sci. Eng.: A 527 (26) (2010) 7092-7098. https://doi.org/10.1016/j.msea.2010.07.081

[2] A. Ekrami, F. Shahri, A. Mirak, Effect of rare-earth elements and quenching wheel speed on the structure, mechanical and thermal properties of rapidly solidified AZ91 Mg melt-spun ribbons[J], Mater. Sci. Eng.: A 684 (27) (2017) 586-591. https://doi.org/10.1016/j.msea.2016.12.105

[3] J.B. Liu, L. Zhang, L. Meng, Effects of rare-earth additions on the microstructure and strength of Cu–Ag composites[J], Mater. Sci. Eng.: A 498 (1-2) (2008) 392-396. https://doi.org/10.1016/j.msea.2008.08.014

[4] K.L. Wang, Q.B. Zhang, M.L. Sun, et al., Rare earth elements modification of laserclad nickel-based alloy coatings[J], Appl. Sur. Sci. 174 (3-4) (2001) 191-200. https://doi.org/10.1016/S0169-4332(01)00017-4

[5] L. Zhang, D. Sun, H. Yu, Characteristics of plasma cladding Fe-based alloy coatings with rare earth metal elements[J], Mater. Sci. Eng.: A 452-453 (2007) 619-624. https://doi.org/10.1016/j.msea.2006.10.142

[6] Z. Zhang, X. Lu, B. Han, J. Luo, Rare earth effect on microstructure, mechanical and tribological properties of CoCrW coatings[J], Mater. Sci. Eng.: A 444 (1-2) (2007) 92-98. https://doi.org/10.1016/j.msea.2006.08.091

[7] M. Yang, Y. Liu, J. Liu, Y. Song, Corrosion and mechanical properties of AM50 magnesium alloy after being modified by 1 wt.% rare earth element gadolinium[J], J. Rare Earths 32 (6) (2014) 558-563. https://doi.org/10.1016/S1002-0721(14)60108-3

[8] Y. Wang, J. He, M. Yan, et al., First-principles Study of NiAl Alloyed with Rare Earth Element Ce[J], J. Mater. Sci. Technol. 27 (8) (2011) 719-724. https://doi.org/10.1016/S1005-0302(11)60132-1

[9] S. Li, H.Y. Song, L. Han, et al., Effect of rare earth element yttrium on migration behavior of twin boundary in magnesium alloys: a molecular dynamics study[J], J. Mater. Res. Technol. 24 (2023) 5991-5999. https://doi.org/10.1016/j.jmrt.2023.04.202

[10] C. Qin, H. Wang, J. Liu, et al., Tuning hydrogen storage thermodynamic properties of $ZrFe_2$ by partial substitution with rare earth element Y[J], Int. J. Hydrogen Energy 46 (2021) 18445-18452. https://doi.org/10.1016/j.ijhydene.2021.03.012

[11] R. Shu, Y. Mao, J.W. Coenen, et al., Microstructure and mechanical properties of W_f/W composites influenced by Y_2O_3 coating[J], Int. J. Refract. Hard Met. 115 (2023) 106322. https://doi.org/10.1016/j.ijrmhm.2023.106322

[12] S. Xing, L. Wang, C. Jiang, et al., Influence of Y_2O_3 nanoparticles on microstructures and properties of electrodeposited Ni–W–Y_2O_3 nanocrystalline coatings[J], Vac. 181 (2020) 109665. https://doi.org/10.1016/j.vacuum.2020.109665

[13] A. Fazi, M. Sattari, M. Strach, et al., CrN–NbN nanolayered coatings for enhanced accident tolerant fuels in BWR[J], J. Nucl. Mater. 586 (2023) 154681. https://doi.org/10.1016/j.jnucmat.2023.154681

[14] M.A. Abdelkareem, T. Wilberforce, K. Elsaid, et al., Transition metal carbides and nitrides as oxygen reduction reaction catalyst or catalyst support in proton exchange membrane fuel cells (PEMFCs)[J], Int. J. Hydrogen Energy 46 (45) (2021) 23529-23547. https://doi.org/10.1016/j.ijhydene.2020.08.250

[15] Y. Ren, J. Jia, X. Cao, et al., Effect of Ag contents on the microstructure and tribological behaviors of NbN–Ag coatings at elevated temperatures[J], Vac. 204 (2022) 111330. https://doi.org/10.1016/j.vacuum.2022.111330

[16] Q. Xie, X. Liu, Z. Zhang, et al., Investigation of mechanical and electronic properties of a novel quaternary transition-metal nitride Ti0.25W0.25V0.25Ta0.25N[J], Mater. Chem. Phys. 310 (2023) 128467. https://doi.org/10.1016/j.matchemphys.2023.128467

[17] J. Yi, J. Xiong, Z. Guo, et al., Growth, mechanical properties, and tribological performance of TiAlN/NbN and NbN/TiAlN bilayer coatings[J], Ceram. Int. 48 (5) (2022) 6208-6217. https://doi.org/10.1016/j.ceramint.2021.11.161

[18] V. Phumzile Mkhwanazi, B. Joseph Babalola, O. Oluremi Ayodele, et al., Densification, microstructure, and mechanical properties of sintered TiAl-NbN

composites[J], Mater. Today: Proceedings (2023). https://doi.org/10.1016/j.matpr.2023.08.001

[19] P.E. Hovsepian, A.A. Sugumaran, M. Rainforth, et al., Microstructure and load bearing capacity of TiN/NbN superlattice coatings deposited on medical grade CoCrMo alloy by HIPIMS[J], J. Mech. Behav. Biomed. Mater. 132 (2022) 105267. https://doi.org/10.1016/j.jmbbm.2022.105267

[20] W. Shao, Y.F. Zhou, L. Zhou, et al., Effect of Ti-doping on peeling resistance of primary M_7C_3 carbides in hypereutectic Fes-Cr-C hardfacing coating and γ-Fe/M_7C_3 interfacial bonding strength[J]. Mater. Des. 211 (2021) 110133. https://doi.org/10.1016/j.matdes.2021.110133

[21] X.Yun, Y.F. Zhou, J. Yang, et al., Refinement of nano-Y_2O_3 on microstructure of hypereutectic Fe-Cr-C hardfacing coatings[J]. J. Rare Earths 33 (06) (2015) 671-678. https://doi.org/10.1016/S1002-0721(14)60469-5

[22] J.B. Wang, T.T. Liu, Y.F. Zhou, et al., Effect of nitrogen alloying on the microstructure and abrasive impact wear resistance of Fe-Cr-C-Ti-Nb hardfacing alloy[J]. Surf. Coat. Technol. 309 (2017) 1072-1080. https://doi.org/10.1016/j.surfcoat.2016.10.029

[23] M. Cheng, M. Liang, H. Liao, First principles study of Ni_3Al/Ni_6Ta_2 interface and electronic properties, Vac. 203 (2022) 111241. https://doi.org/10.1016/j.vacuum.2022.111241

[24] Y. Li, W. Chen, Y.-k. Li, et al., Revealing the interface energy and electronic properties of NbN/α-Fe in shipbuilding steels[J], Mater. Today Commun. 35 (2023) 105852. https://doi.org/10.1016/j.mtcomm.2023.105852

[25] Kresse G, Ab initio molecular dynamics for liquid metals[J]. J. Non. Cryst. Solids 192-193 (1995) 222-229. https://doi.org/10.1016/0022-3093(95)00355-X

[26] J. P. Perdew, K. Burke, M. Ernzerhof., Generalized gradient approximation made simple[J]. Phys. Rev. Lett. 77 (18) (1996) 3865. https://doi.org/10.1103/PhysRevLett.77.3865

[27] P. E. B löchl, Projector augmented-wave method[J], Phys. Rev. B, 50(24) (1994) 17953. https://doi.org/10.1103/PhysRevB.50.17953

[28] B.L. Bramfitt, The effect of carbide and nitride additions on the heterogeneous nucleation behavior of liquid iron[J], Metall. Trans. 1 (1970) 1987–1995. https://doi.org/10.1007/BF02642799

[29] Z. Shi, S. Liu, J. Guo, et al., Investigation on heterogeneous nucleation substrate of Y_2O_3 as NbC in hypereutectic Fe–Cr–C hard facing coating by experiment and firstprinciples calculation[J]. J. Mater. Sci. 54 (14) (2019) 10102-10118. https://doi.org/10.1007/s10853-019-03548-y

[30] Boettger J C. Nonconvergence of surface energies obtained from thin-film calculations[J], Phys. Rev. B 49 (23) (1994) 16798. https://doi.org/10.1103/PhysRevB.49.16798

[31] F. Chen, H. Jiang, Y. Zhang, et al., First-principles calculation of bonding and hydrogen trapping mechanism of Fe_3C/α-Fe interface[J], J. Mater. Res. Technol. 26 (2023) 6782-6793. https://doi.org/10.1016/j.jmrt.2023.09.074

[32] J. Wang, J. Yang, C. Wang, et al., First-principles calculation on $LaAlO_3$ as the heterogeneous nucleus of TiC[J]. Comp. Mater. Sci. 101 (2015) 108-114. https://doi.org/10.1016/j.commatsci.2015.01.024

[33] Z. Shi, S. Liu, Y. Gao, et al., Mechanism of Y_2O_3 as heterogeneous nucleus of TiC in hypereutectic Fe-Cr-C-Ti- Y_2O_3 coating: first principles calculation and experiment research[J]. Mater. Today Commun. 13 (2017) 80-91. https://doi.org/10.1016/j.mtcomm.2017.09.002

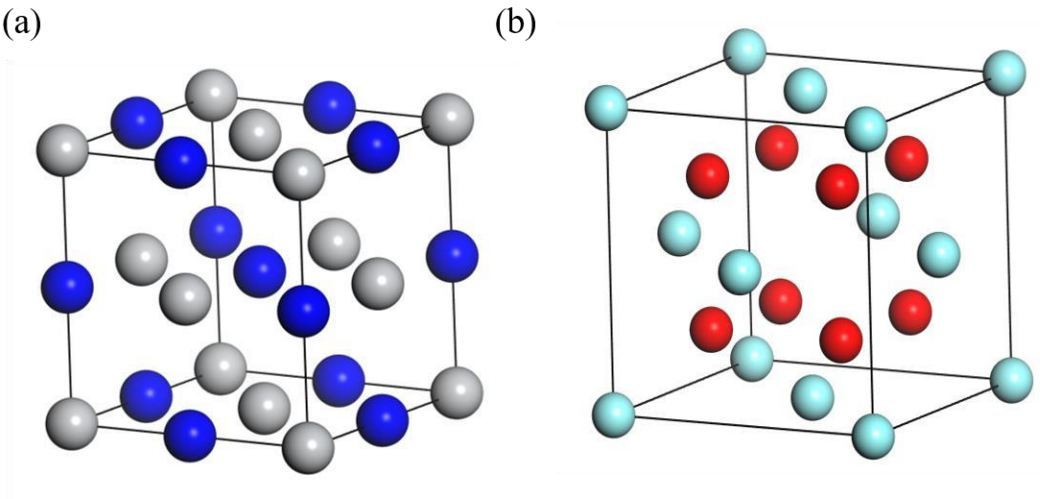

Fig. 1 Crystal structure of NbN and Y_2O_3

(a) NbN; (b) Y_2O_3

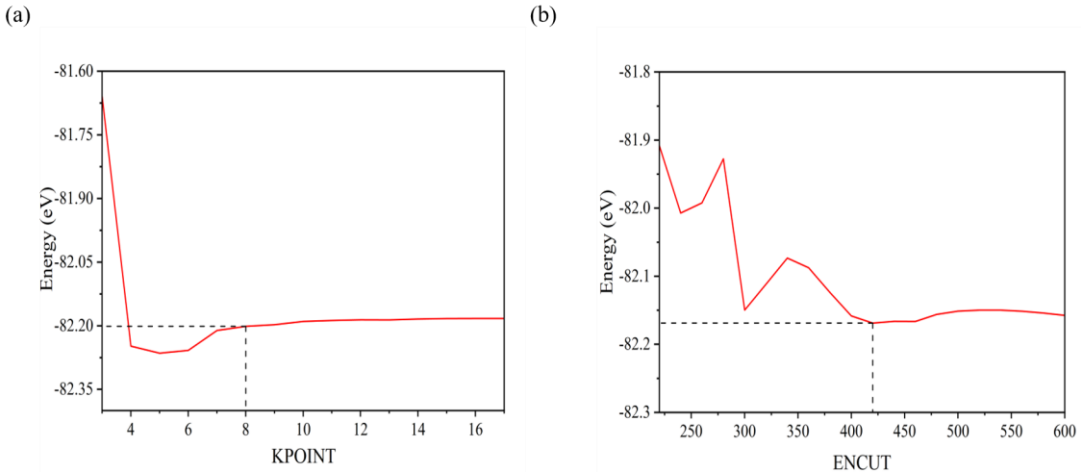

Fig. 2 K point and Encut of NbN

(a) K point; (b) Encut

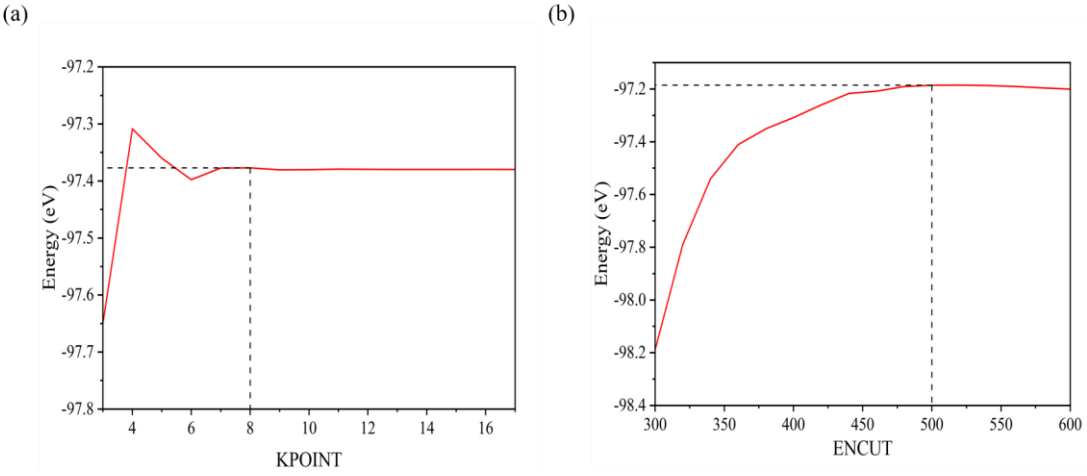

Fig. 3 K point and Encut of Y_2O_3

(a) K point; (b) Encut

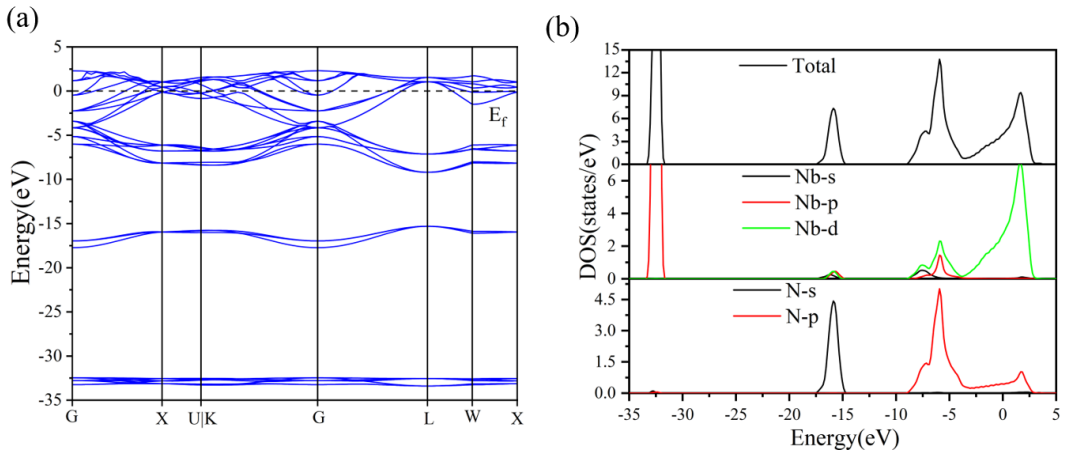

Fig. 4 Bulk phase properties of NbN

(a) Band structure diagram; (b) DOS

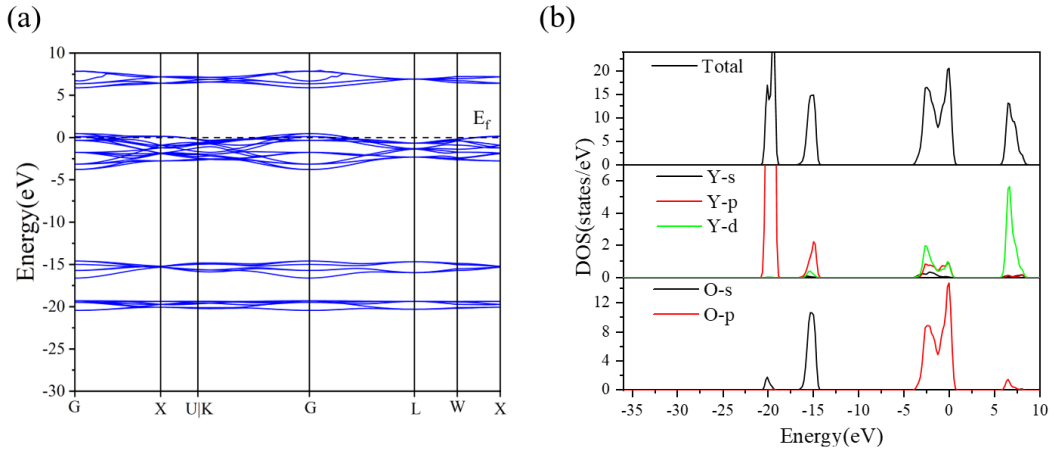

Fig. 5 Bulk phase properties of Y_2O_3

(a) Band structure diagram; (b) DOS

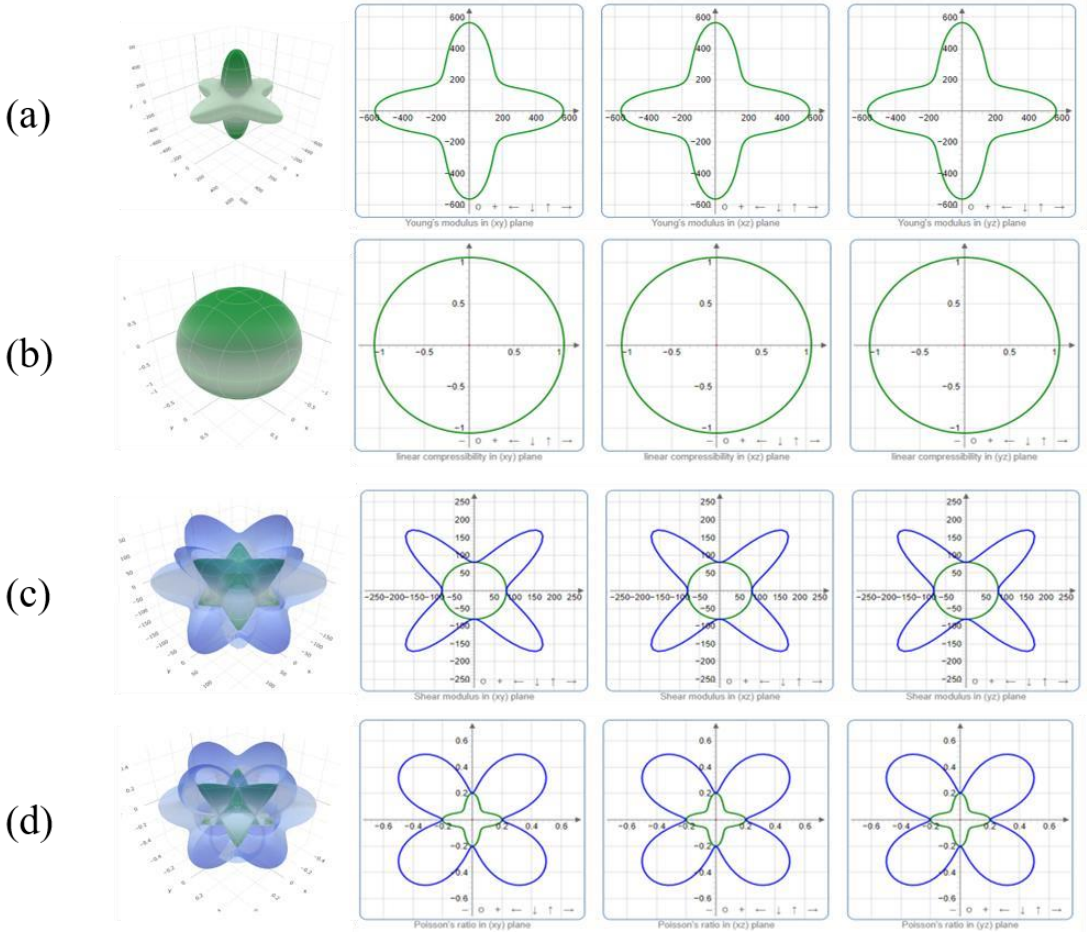

Fig. 6 3D and 2D maps of the NbN's elastic anisotropy

(a) Young's modulus; (b) Linear coefficient; (c) Shear modulus; (d) Poisson's ratio

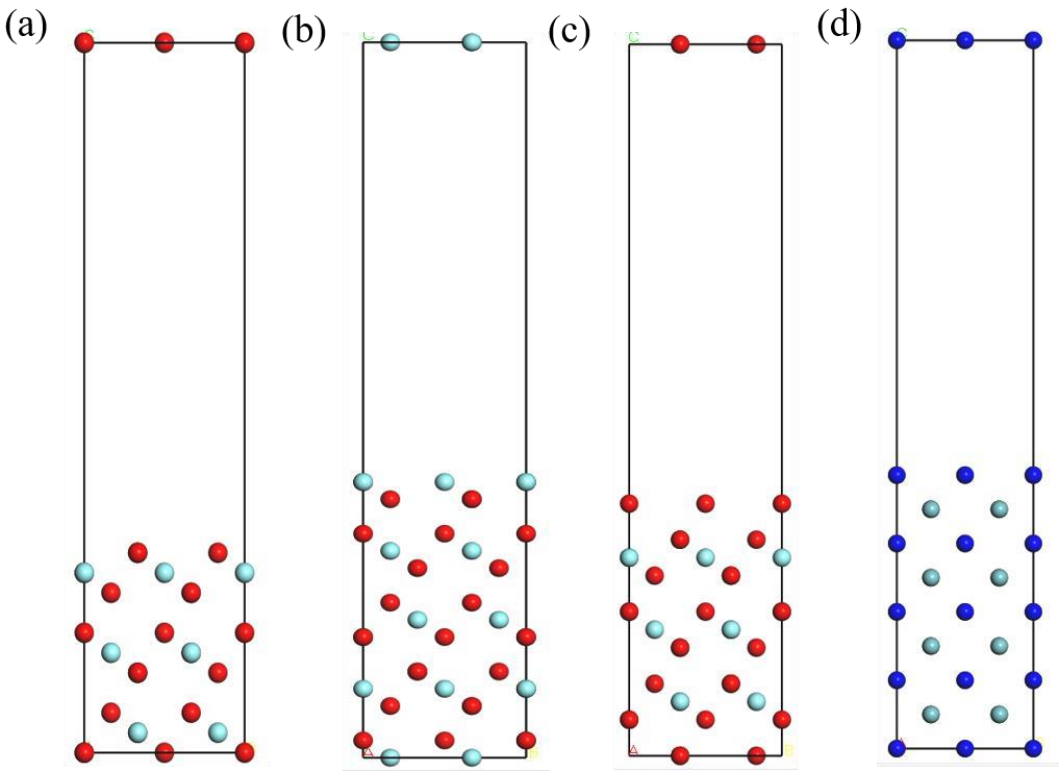

Fig. 7 Surface models of Y_2O_3 and NbN planes

(a) Y_2O_3(111) surface model of Y-terminated; (b) Y_2O_3(111) surface model of O1-terminated;

(c) Y_2O_3(111) surface model of O2-terminated; (d) NbN(110) surface model

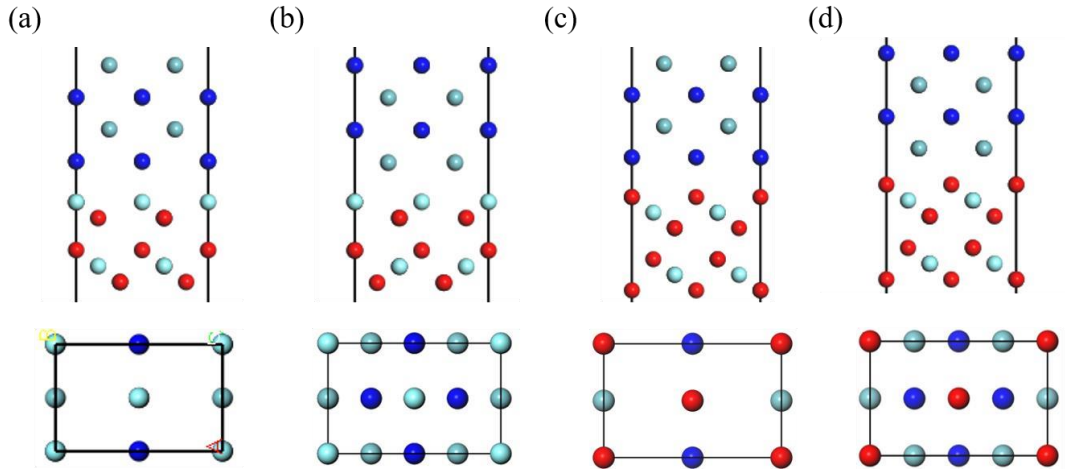

Fig. 8 Four interface models of Y_2O_3(111)/NbN(110) interface (a) Y-NbN Ⅰ; (b) Y-NbNII; (c) O-NbN Ⅰ; (d) O-NbNII

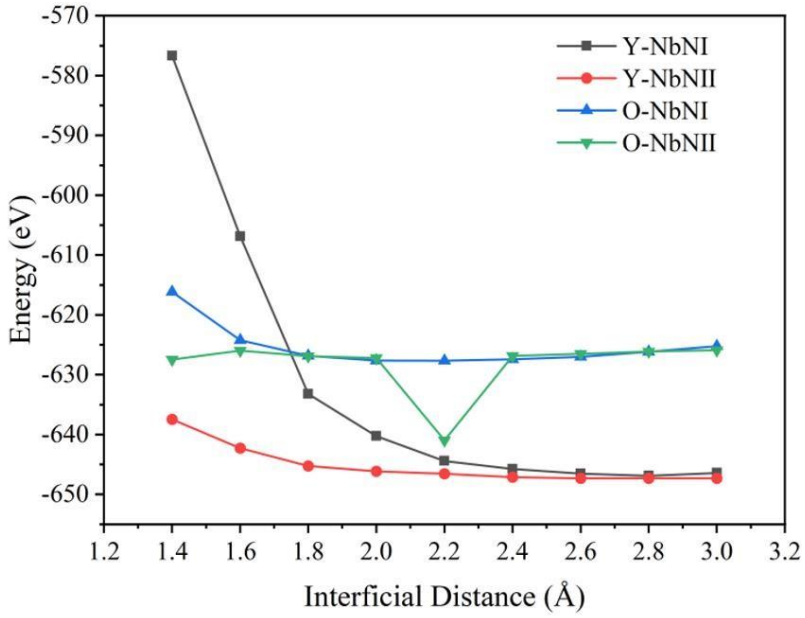

Fig. 9 Energy of four interfacial models with different interfacial spacing

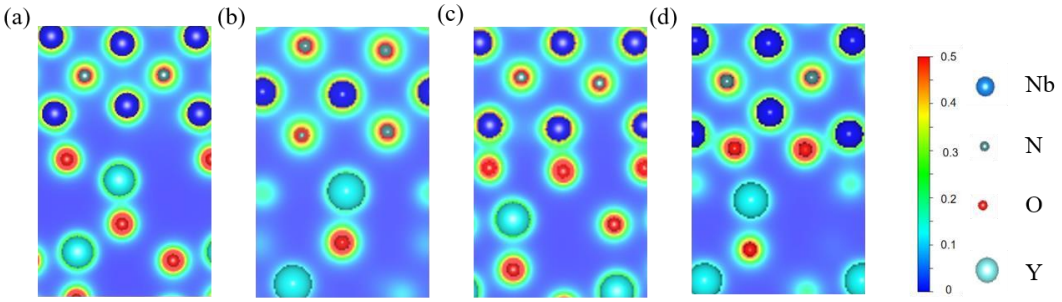

Fig. 10 Charge densities of the Y_2O_3(111)//NbN(110) interface models (a) Y-NbN Ⅰ; (b) Y-NbNII; (c) O-NbN Ⅰ; (d) O-NbNII

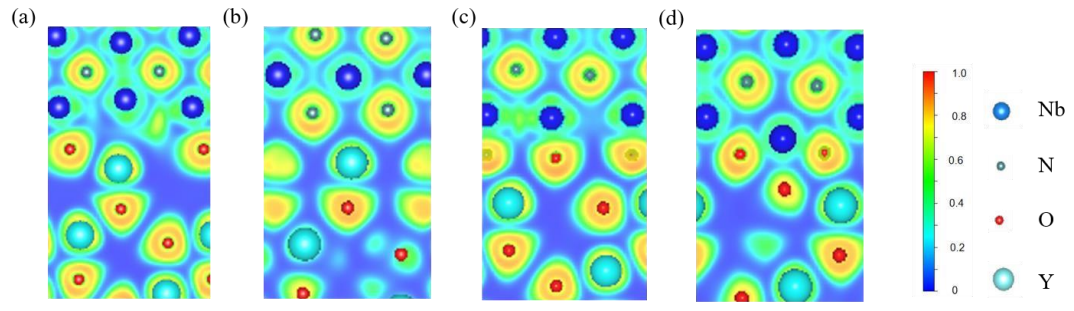

Fig. 11 ELF distributions of the Y_2O_3(111)//NbN(110) interface models

(a)Y-NbN Ⅰ; (b) Y-NbNII; (c) O-NbN Ⅰ; (d) O-NbNII

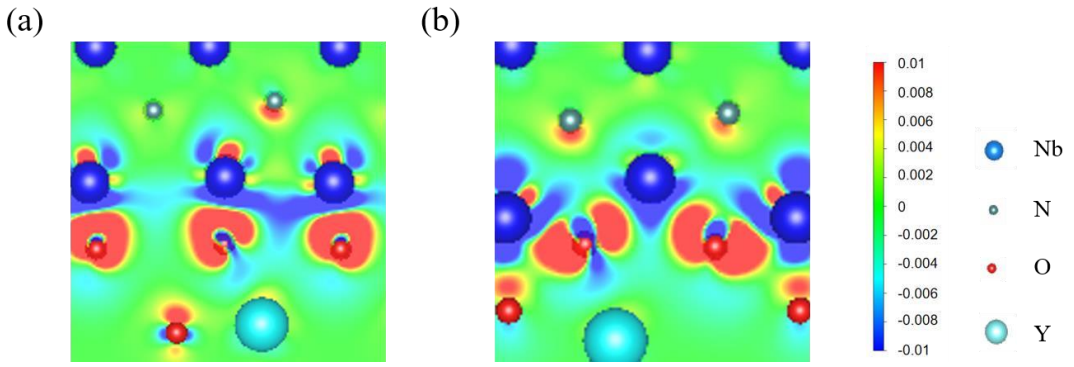

Fig. 12 Differential charge density of the Y_2O_3(111)//NbN(110) interface models

(a) O-NbN Ⅰ; (b) O-NbNII

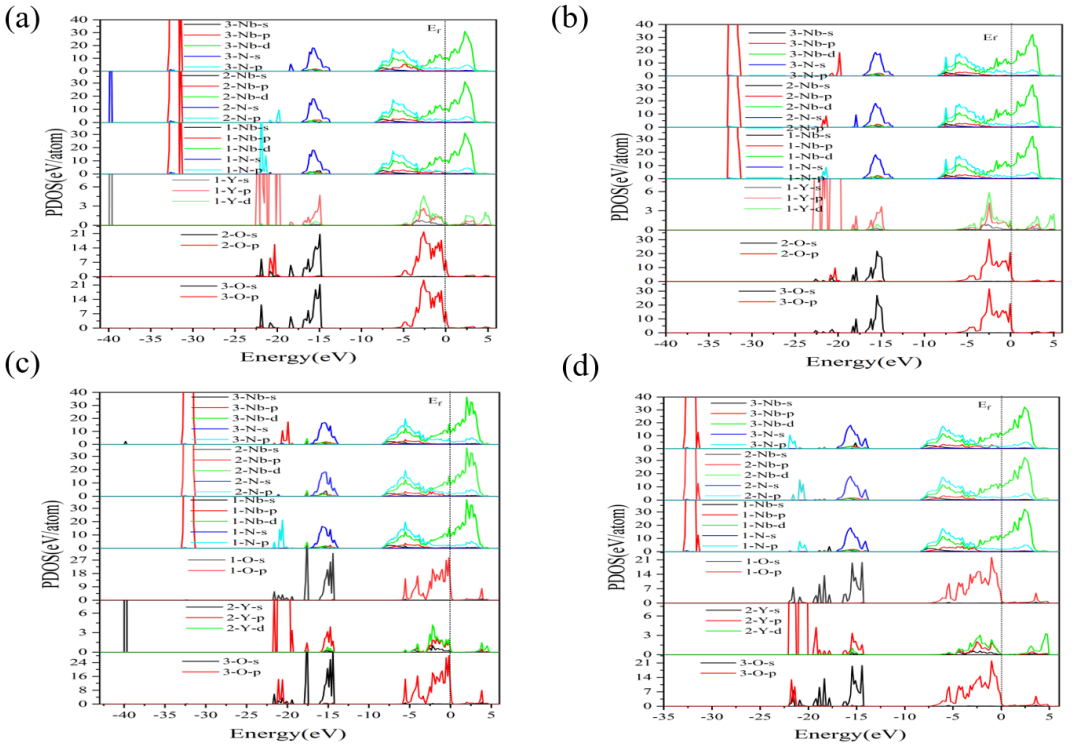

Fig. 13 PDOS of the Y_2O_3(111)//NbN(110) interface models

(a)Y-NbN Ⅰ; (b) Y-NbNII; (c) O-NbN Ⅰ; (d) O-NbNII